D Zhao et al 2022 Phys. Scr. **97** 024005, doi:10.1088/1402-4896/ac4a93

Investigation of boron distribution and material migration on the W7-X divertor by picosecond LIBS

D. Zhao [a, b, *], S. Brezinsek [b], R. Yi [b], J. Oelmann [b], L. Cai [a], F. Wu [a], G. Sergienko [b], M. Rasinski [b], M. Mayer [c], C.P. Dhard [d], D. Naujoks [d], and the W7-X team [d§]

[a] Southwestern Institute of Physics, P.O.Box 432, Chengdu, Sichuan, 610041, China

[b] Forschungszentrum Jülich, Institut für Energie- und Klimaforschung - Plasmaphysik, Partner of the Trilateral Euregio Cluster (TEC), 52425 Jülich, Germany

[c] Max-Planck-Institut für Plasmaphysik, 85748 Garching, Germany

[d] Max-Planck-Institut für Plasmaphysik, 17491 Greifswald, Germany

[§] See the author list of T Klinger et al, Nuclear Fusion 59 (2019) 112004

A B S T R A C T

One set of horizontal target elements of the Test Divertor Units (TDU), retrieved from the Wendelstein 7-X (W7-X) vessel after the end of second divertor Operation Phase (OP1.2B) in Hydrogen (H), were investigated by picosecond Laser-Induced Breakdown Spectroscopy (ps-LIBS). The Boron (B) distribution, H pattern and the material erosion/deposition pattern on these target elements were analyzed with high depth resolution and mapped in the poloidal direction of W7-X. From the spectroscopic analysis, B, H, Carbon (C) and Molybdenum (Mo) were clearly identified. A non-uniformly distributed B pattern on these divertor target elements was determined by the combination of B layer deposition during the three boronizations and W7-X plasma operation with multiple erosion and deposition steps of B. Like the TDU, the analyzed target elements are made of fine grain graphite, but have two marker layers which allow us to determine the material migration via the ps-LIBS technique. Two net erosion zones including one main erosion zone with a peak erosion depth of 6.5 μm and one weak erosion with a peak erosion of 1.3 μm were determined. Between two net erosion zones, a net deposition zone with width of 135 mm and a thickness up to 3.5 μm at the peak deposition location was determined by the ps-LIBS technique. The B distributions are correlated with the erosion/deposition pattern and the operational time in standard magnetic configuration of W7-X in the phases after the boronizations. The thickness of the containing B layer on these target elements also correlates with the erosion/deposition depth, in which the thickness of the containing B layer varies spatially in poloidal direction between 0.1 μm and 6 μm. Complementary, Focused Ion Beam combined with Scanning Electron Microscopy (FIB-SEM) was employed also to verify and investigate the deposition layer thicknesses at typical net erosion and net deposition zones as well as to identify the three boronizations in depth.

Keywords: W7-X Divertor, material migration, boron distribution, erosion pattern, picosecond LIBS

[*] Corresponding author. *E-mail address*: zhaodongye@swip.ac.cn

[§] See the author list of T Klinger et al for the W7-X team (https://doi.org/10.1088/1741-4326/ab03a7)

1. Introduction

The superconducting stellarator Wendelstein 7-X (W7-X), which is equipped with graphite divertors, baffles and shields, has completed two divertor Operational Phases (OP) with an inertially cooled graphite divertor called Test Divertor Unit (TDU) [1, 2]. In the second phase (OP1.2B), three boronizations by Helium (He) glow discharge (GDC) with 10% B_2H_6 diluted in 90% He were performed with four weeks of interval and an accumulated GDC time of 14 hours, in order to improve wall conditions and plasma performance [3, 4]. As results of the boronizations, both the oxygen to hydrogen flux ratio and the carbon to hydrogen flux ratio at the divertor decreased, which was obtained from in-situ emission spectroscopic measurements [5, 6].

Several specially designed marker Plasma-Facing Components (PFCs) installed in the Test Divertor Unit (TDU), were employed as exchangeable divertor target elements to investigate the material migration, boron distribution and their relationship on the W7-X divertor [2, 7]. These TDU target elements, dedicated in the following as marker samples, consist of three layers: fine-grain graphite as substrate, 0.2–0.4 μm Mo as intermediate layer (as a marker), 5-10 μm C (to study the C migration) as top layer. The marker layers on the target elements were produced by Combined-Magnetron Sputtering with Ion Implantation (CMSII). The detailed information about marker layers and CMSII could be found in [7, 8]. Due to these marker layers, these TDU target elements could be used to determine the erosion/deposition pattern of the divertor by ion beam analysis and laser beam methods [9, 10].

Laser-Induced Breakdown Spectroscopy (LIBS) due to its unique advantages, had been proposed as a potential candidate for *in-situ* investigations of Plasma-Wall Interaction (PWI) in nuclear fusion devices [11-13]. It also has the benefits in lateral and depth resolution analysis of bulk samples by LIBS technique according to the atomic emission spectroscopy and number of laser ablation pulses [14]. In the LIBS technique, the absolute ablation depth in the LIBS measurement can be calculated when the ablation rate of measured material is determined and the number of laser pulses is counted [15, 16]. This determination of absolute ablation depth allows the quantification of layered materials by the LIBS method [14, 15, 17]. Currently, to demonstrate LIBS capabilities in nuclear fusion device, the in-situ LIBS had been installed and employed to diagnose the PFCs in several tokamak devices, like TEXTOR [18], EAST [19], HL-2M [20], FTU [21], and proposed for future application in W7-X [22, 23]. For impurities deposition analysis on the PFCs by LIBS, in 2007, Grisolia et al. reported the laser-based applications for co-deposited layers measurement [24]. Schweer et al. showed an implementation for wall surface characterization and condition using laser-based techniques in 2009 [25]. J Karhunen et al. investigated the applicability of LIBS for *in-situ* monitoring of deposition and retention on ITER-like wall [26]. GS. Maurya et al. analyzed the deposited impurity material on the surface of the optical window and limiter of the Tokamak [27, 28]. P. Paris et al. investigated the erosion, deposition, and fuel retention on PFCs in ASDEX upgrade by LIBS [29]. S. Almaviva et al. used a double pulse LIBS method to measure the surface elemental composition and fuel retention [30]. L. Sun et al. studied the deuterium retention and carbon deposition on shaped tungsten castellated blocks exposed in KSTAR by LIBS [31]. In these works, the excitation source of laser produced plasma is nanosecond laser. Exploiting the fact that picosecond LIBS (ps-LIBS) has the capacity of enhanced depth-resolution, a small mass removal and a reduction of the heat-affected zone, it is becoming a preferable choice for the PFCs diagnostic in nuclear fusion devices [32, 33]. E. g, AM. Roldán et al. reported a comparison between the ps-LIBS and nanosecond LIBS (ns-LIBS) for PFCs characteristics [34]. C. Li et al. had studied an elemental depth analysis of limiter graphite tiles of W7-X by ps-LIBS method [35].

In this work, the material migration and boron distribution of the horizontal target element TM2h6 of the TDU, located at upper Half Module in sector 1, so-called HM 1u (**H**alf **M**odule abbreviate HM, sector **1** abbreviate 1, and **u**pper location abbreviate **u**) in W7-X, was analyzed ex-situ by the ps-LIBS technique. TM2h6 was target module 2, horizontal, target element 6. The distributed B pattern on the TM2h6 divertor target element was determined. Due to the marker layers on TDU target elements, the depth profile of the Mo marker layer was applied to determine the material migration and further erosion and deposition patterns. As a result, the material migration and boron distribution which are representative for the whole horizontal target of the uncooled graphite TDU in W7-X are obtained [36]. Moreover, a combination of Focused Ion Beam and Scanning Electron Microscopy (FIB-SEM) was applied to characterize the local erosion and deposition on the TM2h6 target element to validate and cross-check the ps-LIBS results.

2. Measured sample and experimental setup

The TM2h6 target element was retrieved from the W7-X vessel after completion of the OP1.2B campaign. This graphite target element was exposed to predominately hydrogen (H) stellarator plasmas after introduction of the boronization [37]. Because that the He GDC for improving wall condition were not necessary any more after boronizations as discussed in [5]. The details of plasma information during OP1.2B such as the magnetic configurations and associated particle and plasma discharge time were summarized in ref [6, 38, 39]. The installed location of TM2h6 was at the horizontal divertor target of HM 1u in W7-X and the exact location is shown in Fig. 1(a). The gap between the horizontal divertor target and vertical divertor target is Pumping Gap (PG) side, the opposite direction is Out Baffle (OB) side. Fig. 1(b) shows the dimension and the photograph of TM2h6 post W7-X plasma exposure. The zero point of the coordinate system of this work is near the PG side and indicated by point A in Fig. 1(b) marked by a black dot. The marker areas of TM2h6, consisting of fine-grain graphite as substrate, 0.2–0.4 μm Mo as intermediate layer and 5-10 μm C layer as top layer, are indicated by the red

boxes in Fig. 1(b). The measurement direction of ps-LIBS is from the PG to the OB which direction corresponds to the poloidal direction of W7-X. The first ps-LIBS measurement position is 2 mm from the zero coordinate. The interval of each ps-LIBS measurement position was 5 mm with an ablation diameter of 1 mm. At each of the 109 poloidal positions, 200 laser pulses in row at one position were carried out to obtain depth-resolved information and thus to determine erosion and deposition zones of TM2h6 target element. As shown in Fig. 1(b), the TM2h6 target element consists of eight individual graphite tiles; further information about the TM2h6 target element nomenclature can be found in ref [10]. The image of one typical TDU graphite tile after W7-X plasma exposure is depicted in Fig. 2(a). The exact area of the marker layer on the graphite tile is shown by the green rectangle in Fig. 2(a). The marker layer design is shown in Fig. 2(b) in which the thickness of Mo interlayer and C top layer are about 0.2-0.4 μm and 5-10 μm, respectively. The detailed information of marker graphite tile and TDU target are described also in our previous works [2].

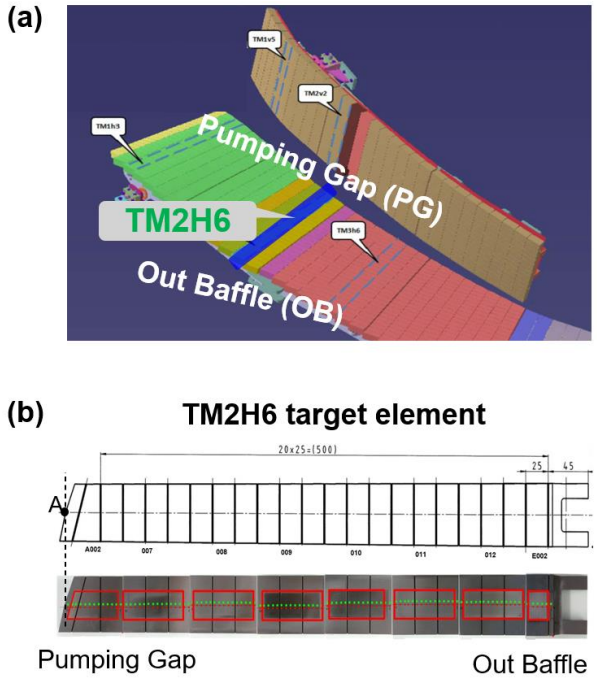

Fig. 1 (a) Schematic representation of the location of the TM2h6 horizontal divertor target element located at TDU half module 1u in W7-X. PG is the direction towards the divertor pumping gap between the horizontal and the vertical target of the TDU, OB towards the out baffle. (b) the dimension and the photograph of TM2h6 post plasma exposure. The zero point of the beginning coordinates in the work is indicated by the point A in Fig. 1(b) marked by black dot. The direction of ps-LIBS measurement is from the PG to the OB which corresponds to the poloidal direction of W7-X.

A schematic diagram of ps-LIBS setup had been represented in our previous works [10, 23]. A picosecond laser (EKSPLA, PL2241, wavelength: 355 nm, pulse width: 35 ps) was employed to produce a laser-induced ablation plasma. A plan-convex quartz lens was applied to focus the laser beam on the measured sample. As result, a laser fluence (F) of 2.3 J/cm^2 on the sample was achieved. The experiments were carried out in a vacuum chamber which was pumped down to 1.2×10^{-7} mbar in 30 minutes and then filled with ultrapure He gas (99.9999%) to 0.7 mbar for the measurement. The laser beam ablated the sample at normal incidence (90±2°). Two spectrometers with the same configuration including one CCD spectrometer (HR2000 Ocean optics, 350 nm to 800 nm) and one high intensity ICCD spectrometer (iStar DH334T-18F, Andor, wavelength range of about 15 nm), were employed to obtain the plasma emission spectra. The overview spectrum was recorded by the CCD spectrometer which provided information about the main concern elements. The ICCD spectrometer was employed to investigate the B distribution due to its benefits of high-resolution. A digital delay generator (DG645) was utilized to synchronize the picosecond laser pulses and these two spectrometers to obtain the spectra.

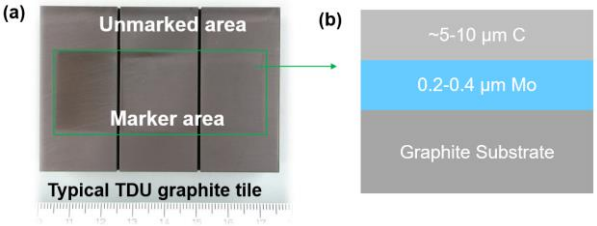

Fig. 2 (a) One typical TDU graphite tile after W7-X plasma exposure. The exact marker layer area is indicated by green rectangle, the outer area of the green rectangle represents the area without marker layers. (b) The schematic design of the marker layers on marker area. There are two marker layers including a Mo interlayer of about 0.2-0.4 μm and a C top layer of 5-10 μm on the graphite substrate.

3. Results and discussions

3.1. Ps-LIBS spectra of TM2h6

Typical LIBS spectra of the TM2h6 target element at different laser pulses at the same spatial location obtained in a crater are shown in Fig. 3. Emission lines of different atomic species like Mo, Na, H, C can be clearly observed and identified by an overview CCD spectrometer and the results are shown in Fig. 3(a). Note that the P4 in the Fig. 3(a) indicates the various emission lines in the different laser pulses due to the limited spectral resolution of the employed CCD spectrometer. However, the emission lines revealed by P4 were not used for data analysis, and thus it will not affect the result interpretations. As shown in Fig. 3(a), the spectral intensities of the observed lines, especially for the Mo atomic lines, vary significantly along with the laser from pulse to pulse and thus at different ablation depths in the target. Combining with the TDU target design shown in Fig. 2, this Mo emission features have been used to determine the absolute erosion/deposition pattern by the ps-LIBS technique. This has been described in detail in ref [17]. In this work, the B ionic emission lines were measured by a high-resolution ICCD spectrometer. The B II 703.02 nm and 703.25 nm lines were

identified and shown in Fig. 3(b). The intensities of B II lines also vary with the laser ablation pulses. It should note that the scale of the emission intensity of laser produced plasma in CCD spectrometer (Fig. 3(a)) and ICCD spectrometer (Fig. 3(b)) is showed by the raw scale. These various scales are caused by the different spectrometers employed. Because the unit of emission intensity of these spectrometers is in **a**rbitrary **u**nits (a. u), this various scale does not affect experimental result explanations in this work.

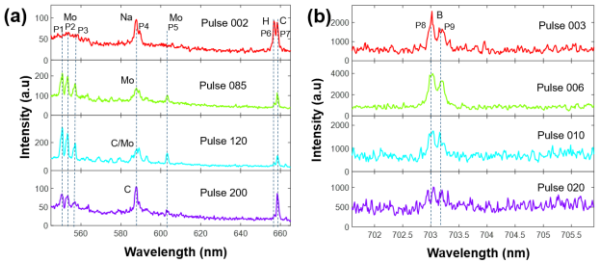

Fig. 3 Typical LIBS emission spectra of the TM2h6 target element with marker layer for different laser pulses. (a) CCD spectrometer results: P1-P3 and P5 indicate the Mo I emission; P4 indicates the spectrally unresolved line emission of Na I at 588.99 nm and 589.59 nm in the 2nd pulse, the Mo I 588.83 nm in the 85th pulse, the unresolved Mo I 588.83 nm and C II 588.97 nm in the 120th pulse, and the C II 588.97 nm in the 200th pulse; P6 indicates the H I emission at 656.27 nm, and P7 indicates the C II at 657.80 nm. (b) ICCD spectrometer results: P8 and P9 indicate the B II 703.02 nm and B II 703.25 nm. The delay time and gate width of ICCD are set as 20 ns and 10 μs, respectively.

3.2. Elemental depth profile of TM2h6

Duo to the installed TDU type target element, TM2h6 target element allow us to investigate the material migration including erosion and deposition. Fig. 4(a), (b) and (c) show the examples of the emission features of C and Mo at the net erosion, low plasma impact and net deposition zones, respectively. In the Fig. 4, the C II emission is obtained as the average of the emission intensities of the C II lines at 426.73 nm and 657.80 nm. The Mo I emission is determined by averaging the emission intensities of the three Mo I lines at 550.67 nm, 553.30nm and 557.04 nm. The averaging has a benefit of enhancing the signal robustness and reducing relative standard deviations of the C and Mo emission caused by the random noise. Moreover, for the H emission, the H I 656.27 line is employed for the spectral analysis. As shown in Fig. 4(b), at the low plasma impact zone, three emission regimes can clearly be identified and assigned as C emission layer, Mo-C emission layer, and substrate graphite. The transition interfaces of these three emission regimes are determined by the intersection of the Mo emission and the signal threshold. This determination method has been described in detail in our previous work [17]. At the net erosion zone shown in Fig. 4(a), the Mo-C emission layer is observed at the start of the laser pulse sequence. This means that the entire top C layer was eroded by W7-X plasma. Indeed, at the peak erosion location, not only the C top layer but also partly the Mo interlayer were eroded in the OP1.2B campaign. This erosion result also was obtained and discussed for the same target element but for a different W7-X campaign in our previous works [9, 10]. At the net deposition zone, the eroded material including the main impurity C combined with other impurities were deposited on the target surface resulting in a thicker top layer. A typical depth profile at this deposition zone is shown in Fig. 4(c), comparing with the zone of low plasma impact the appearance of Mo-C emission layer delay about 32 laser pulses. This implies that the impurities deposited on the target surface and resulted in a deposition layer with a thickness of up to the ablation depth equivalent to 32 laser pulses. The ablation rate of the C layer after the W7-X plasma exposure was measured to be about 108 ± 0.5 nm/pulse in our previous work [17]. By using this ablation rate and combining with the 32 laser pulses, the deposition thickness of the location as shown in the Fig. 4(c) can be calculated to be about 3.5 μm. Based on the depth profile of C and Mo, the erosion and deposition patterns and thus material migration could be determined.

Fig. 4(d), (e) and (f) show the B depth profile at the net erosion zone, the zone of low plasma impact and the net deposition zone, respectively. The thicknesses of the B rich layer (corresponding to the last laser pulses with ionic B line emission) vary at the erosion, low plasma impact and deposition zones, in which the thickness of B rich layer at deposition zone (Fig. 4(f)) is thicker than that in erosion zone (Fig. 4(d)) and low plasma impact zone (Fig. 4(e)).

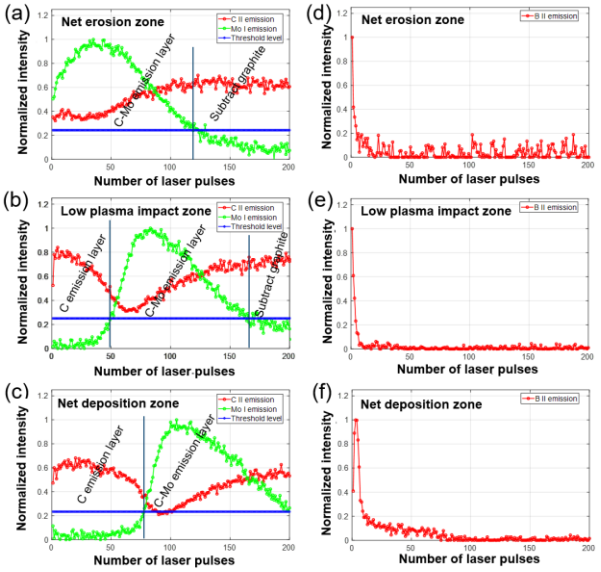

Fig. 4 The C, Mo and B emission as the function of laser pulses at net erosion zone shown in (a) and (d), zone of low plasma impact shown in (b) and (e) and net deposition zone shown in (c) and (f), respectively. At low plasma impact zone shown in Fig. 4(b), three emission regimes can clearly be identified and assigned as C emission layer, Mo-C emission layer, and substrate graphite.

3.3. Boron distribution and erosion and deposition patterns

As discussed in section 3.2 and shown in Fig. 4, the erosion and deposition on the TM2h6 target element can be

qualitatively correlated with the Mo depth profile with increasing number of laser pulses. In this work, the TM2h6 target element was scanned by ps-LIBS measurement at the center of the tile along the toroidal direction. The first ps-LIBS measurement location is at 2 mm from the point A shown in Fig. 1(a). The distance between two ps-LIBS measurement locations is 5 mm. At each of the 109 poloidal measurement locations, 200 laser pulses were carried out to obtain the Mo depth profiles which were used to map the erosion and deposition patterns. The results are shown in Fig. 5, the TM2h6 target element and the measurement direction indicated by a black arrow are shown in Fig. 5(a). The qualitative erosion/deposition pattern of the TM2h6 target element is shown in Fig. 5(b). The discontinuity of the profile of Mo emission in the poloidal direction reflects the gaps in the marker layer of TM2h6 target element which consist of 8 individual graphite tiles. The immediate appearance of Mo emission at the TM2h6 target element surface reveals the area of strong net erosion. The appearance of the Mo-C emission layer delay than that at low plasma impact location in the axis of laser pulse number represents the deposition. A detailed procedure for the determination of erosion and deposition by ps-LIBS has been shown in Fig. 4 in the section 3.2 and also described in our previous work in ref [17].

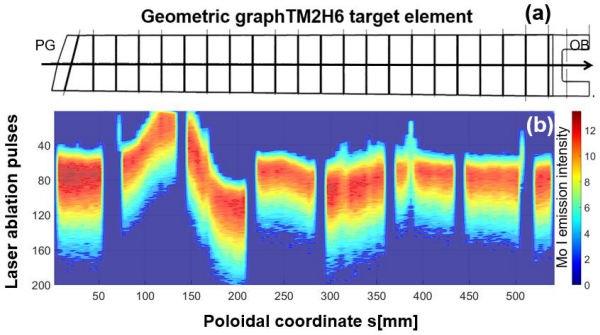

Fig. 5 (a) Schematic representation of the TM2h6 target element. The black arrow indicates the measurement location and direction which is from PG to OB. (b) Depth profile of the Mo atomic line emission in poloidal direction at the measurement locations.

Since the qualitative erosion and deposition patterns were obtained, combining the laser ablation rates of C emission layer, C-Mo emission layer, and substrate graphite, the absolute erosion and deposition pattern can be determined, quantitively. In our previous work, the ablation rates of the C emission layer, C-Mo emission layer, substrate graphite have been determined to be 108 ± 0.5 nm/pulse, 44 ± 2.8 nm/pulse and 30 ± 3.8 nm/pulse, respectively [17]. Combining these values, the absolute erosion and deposition pattern along the poloidal direction are determined and shown in Fig. 6(b). The black dots with black lines represent the absolute erosion and deposition depth at the different poloidal coordinates (s). Erosion has a negative value (-) and deposition has a positive sign (+). As result, two net erosion zones near the strike lines were observed. The main net erosion zone spans from s = 47 mm to 172 mm in poloidal coordinate. The peak erosion depth is about 6.5 µm and its position is located around s = 132 mm. This result reflects the first (inner) strike line location on TM2h6 target element in the dominant standard divertor configuration which was used about 53% of the experimental time in OP1.2B [6, 36]. A weak net erosion zone between s = 322 mm to s = 402 mm in the poloidal direction is also detected. At this weak net erosion zone, the erosion depth is up to 1.3 µm and the peak erosion position is near s = 357 mm. Two potential effects contribute to and produce this weak net zone. Firstly, this may relate with the secondary (outer) strike line of the standard divertor configuration on the TM2h6 divertor target [6, 9, 40]. Secondly, due to the rather broad weak net zone and lie around s = 357 mm, this also relate with the low iota configuration of W7-X discharge. The positions of the strike lines and duration of the low iota configuration were summarized in [36]. Moreover, a relatively wide with multi-elements mixed net deposition zone next to the main strike line close to the PG and between the two net erosion zones is also determined by ps-LIBS. The deposition zone extends from s = 172 mm to s = 307 mm in the poloidal direction, which could reflect the location of the O-Point at the island divertor for standard divertor configuration of W7-X [36]. The thickness of the deposition layer is up to about 3.5 µm at the peak deposition location (s = 202 mm). To show the erosion and deposition zones on the TM2h6 target element, the schematic of the TM2h6 target element marked with different colors (light red indicates the erosion zones, light green responds the deposition area) is represented in Fig. 6(a).

The absolute patterns of the locations containing H and B in the poloidal direction are also determined and the results are shown in Fig. 6(c) and (d). The H pattern in the poloidal direction matches well with the erosion/deposition pattern in which the erosion-dominated area, particularly at the strong erosion zone in the region from the s = 107 mm to s =152 mm, shows a lower containing H fuel depth and lower H emission intensity when compare with the strong deposition area. The reduction of H retention in the erosion-dominated area was mainly caused by the high surface temperature at those locations during the W7-X discharge which was discussed in our previous works [10, 41]. Conversely, at the net deposition zone, a thicker H fuel depth (up to 6 µm at the peak deposition location) and higher H emission intensity are observed. H fuel retention is produced by the implantation and co-deposition with B and C. The strongest fuel retention is linked to the co-deposition process where H is embedded in the co-deposition layer mixed with B and C in a relatively thick layer. This observation confirms our previous investigation on the similar TDU target element after the first divertor Operation Phase (OP1.2A) of W7-X [17]. On the other hand, it also was studied and discussed in the previous work by combining the Laser-Induced Ablation-Quadrupole Mass Spectrometry technique [42].

As shown in Fig. 6(d), a non-uniformly distributed B pattern on the TM2h6 target element is detected in the poloidal direction. Combining this information with Fig. 6(b), the distribution of B and the erosion/deposition pattern are qualitatively in good agreement, in which the strong net deposition zone, particularly in the region from the s = 172 mm

to s = 225 mm, shows a thicker B-containing layer and the strong net erosion zone in the region from the s = 107 mm to s = 152 mm shows a no or a much thinner B-containing layer. Indeed, the thickness of the B-containing layer on TM2h6 target element varies spatially in poloidal direction between 0.1 µm (peak erosion location) and 6 µm (peak deposition location) in the LIBS measurement. At the weak erosion area between s = 322 mm to s = 402 mm in the poloidal direction, the B-containing layer is not as obvious as B pattern in the main net erosion area. The B-containing layer at weak net erosion area is little lower than that at the net deposition area. One potential reason is that totally three boronizations were carried out in the OP1.2B campaign of W7-X and the deposited B in each boronization had been not completely eroded by the subsequent W7-X stellarator plasma in the weak erosion before next boronization. This effect may result that the ex-situ ps-LIBS method could not reveal the B pattern on the weak erosion area completely due to the cumulative boronizations with multiple erosion and deposition steps. For the investigation of B pattern at the weak erosion area, an in-situ LIBS technique which had been planned in W7-X [22] can be considered a superior option.

It should be stressed, B in both erosion zone and deposition zone is not a film-like structure, but only the area where B can be identified mixed with C. This pattern is caused by the combination of B deposition during the three boronizations (He GDC with 10% B_2H_6) and W7-X plasma in main H operation in OP1.2B with multiple erosion and deposition steps. Thus, the pattern correlates with the net material migration pattern integrated over the campaign shown in Fig. 6(b). Moreover, as shown in Fig. 4(d), (e) and (f) for the depth profile of B, compared with net erosion zone, the B emission can last more laser pulses at the zone with low plasma impact and the net deposition zone. Especially at the net deposition zone, the B emission increases in the first pulses and then decreases with increasing pulse number. This observation could provide a support that the containing B layer at the net deposition zone might be produced by the combination of three boronizations and multiple erosion and deposition steps during W7-X plasma operation.

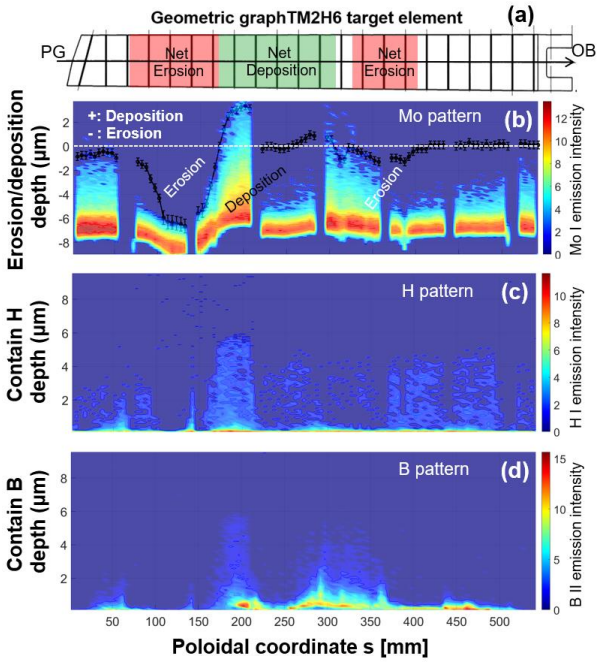

Fig. 6 (a) Schematic representation of the TM2h6 target element, the marked areas filled with light red color indicate the erosion zones, the marked area filled with light green color represent the deposition area. (b) The Mo pattern corresponding as net erosion/deposition depth of target element TM2h6 in poloidal direction in OP 1.2B campaign for the center scan line of ps-LIBS indicated by black arrow in Fig. 6(a). The black dots and lines represent the net erosion/deposition depth. Erosion has negative value and deposition has the positive sign. (c) and (d) H and B patterns in poloidal direction for the center scan line of ps-LIBS, the ordinate indicates the depth containing the H and B. The origin of the poloidal coordinate (s = 0 mm) is defined as the very top of the PG side and also was indicated by point A in Fig. *1*(b).

3.4. Characterization of TM2h6 by FIB-SEM

The FIB-SEM was applied to characterize the surface morphology and cross-sections of the net erosion zone and the net deposition zone on the TM2h6 target element after OP1.2B. The chosen measurement locations are indicated by blue dots named as P01 and P02 in Fig. 7(a). The surface morphology after W7-X plasma exposure of the net erosion zone and the net deposition zone are shown in Fig. 7(b) and Fig. 7(d), respectively. The typical cross-sections at the net erosion zone and the net deposition zone are shown in Fig. 7(c) and Fig. 7(e), respectively. At the net deposition zone (Fig. 7 (e)), based on the internal microstructure and its components, a clear deposition layer is identified by the FIB-SEM technique. The interface between deposition layer and top C layer is indicated by the red dotted line in Fig. 7 (e). In the 11.5 µm wide measurement window of the FIB-SEM image, the thickness of deposition layer at the location 2 mm away the peak deposition location (s = 202 mm) is determined to be in the region form 2.05 - 3.65 µm. This confirms in principle the ps-LIBS results in the determination of the deposition layer thickness in which the thickness is up to about 3.5 µm at the peak deposition location. Here, one should note that the diameter of the ablated crater in the ps-LIBS measurements is about 1 mm which is 87

times larger than the FIB-SEM image window. The determination of the deposition thickness by ps-LIBS is an average of amount cases of the deposition layer thickness, e. g. one case shown in Fig. 7 (e). This averaging effect has been discussed in our previous work [17]. Below the deposition layer mainly made of B, C and H, the C top layer also can be identified clearly in Fig. 7 (e). Moreover, Energy Dispersive X-Ray Analysis (EDX) was carried out at the cross-section in the deposition zone to assess and identify the three boronizations. Three separated broad B peaks are visible in depth of the FIB cutting location and the containing B layer is up to about 6 μm thick. This confirms the gettering process of B and the further detail are given in the overview paper [36].

At the erosion zone (Fig. 7(b)), not only the top C marker layer, but also a small part of the Mo interlayer was eroded by the W7-X plasma impact during OP1.2B and most likely caused by C impurity ions. Moreover, the surface roughness or morphology at the net erosion zone (Fig. 7(b) and (c)) is considerably smoother than the initial marker coated target element indicated by the Mo interlayer following the morphology of the substrate graphite surface shown in Fig. 7(c) and the net deposition zone shown in Fig. 7(e). This observation also was depicted in our previous work [9, 17]. Indeed, the net erosion zone has done the multiple erosion and deposition processes under shallow angle plasma impact. This could result as a smearing effect and then reduce the surface roughness.

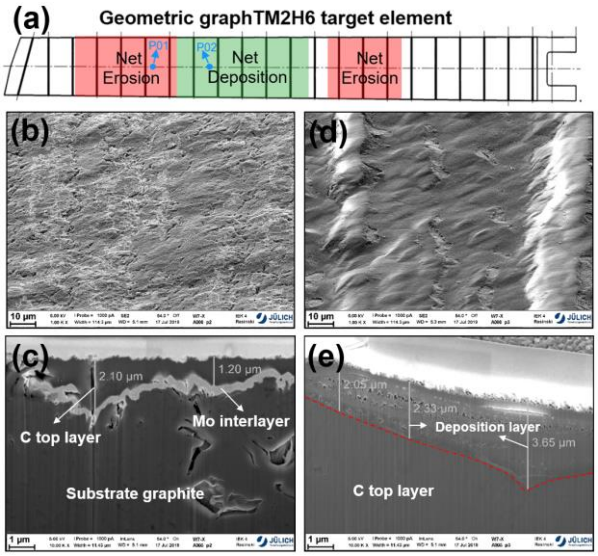

Fig. 7 (a) The schematic of the TM2h6 target element. P01 and P02 represent two typical locations which are analyzed by FIB-SEM. P01 and P02 are located at net erosion zone and net deposition zone, respectively. (b) and (d) The surface morphology after W7-X plasma exposure at the net erosion zone and the net deposition zone, respectively. (c) Cross-section of the marker layer on top of the target element TM2h6 at net erosion zone. The top C marker layer and part of Mo interlayer were eroded and the surface roughness was reduced due to W7-X plasma impact during the OP1.2B campaign. (e) Cross-section of the marker layer on top of the target element TM2h6 at net deposition zone. A clear deposition layer in the thickness of 2.05-3.65 μm is identified above on the top C layer. Blow the deposited layer, the C marker layer is also identified.

4. Conclusion

One dedicated target element of type TM2h6 installed in the horizontal target of HM 1u and retrieved after the end of OP1.2B of W7-X, was investigated by ps-LIBS in order to determine the local plasma-surface interaction processes. General material erosion, transport, and deposition, B distribution and hydrogen retention caused by W7-X plasma impact was studied. The TM2h6 target element was scanned by the ps-laser with a lateral resolution of 5 mm in a line in poloidal direction from the pumping gap to the outer baffle side. Mo, Na, H, C and B emission lines were identified and observed clearly in ps-LIBS measurements. Two net erosion zones including one main erosion zone with width of 125 mm and a peak erosion depth of 6.5 μm and one weak erosion with width of 80 mm and peak erosion depth of 1.3 μm were determined. The peak erosion location of the main net erosion zones on TM2h6 is located at s = 132 mm, which relate with the first (inner) strike line positions in standard magnetic divertor configuration in W7-X. The weak net erosion zone is rather broad and peak erosion location is at s = 357 mm. This may relate with not only the secondary (outer) strike line in standard magnetic divertor configuration but also the strike line in low iota configuration in W7-X. Between these two net erosion zones, a net deposition zone extending from s = 172 mm to 307 mm in the poloidal direction was also identified and the thickness of the deposition layer amounts at the peak deposition location (s = 202 mm) up to about 3.5 μm. A non-uniformly distributed B pattern on TM2h6 target elements was determined and the thickness of the containing B layer varied spatially in poloidal direction between 0.1 μm and 6 μm in the poloidal direction of W7-X. The distribution of B correlates with the general erosion/deposition pattern. The B distribution is caused by a combination of B deposition during the three boronizations and multiple erosion and deposition steps during normal W7-X operation. FIB-SEM was applied also to investigate the net erosion zone and net deposition zone. The thickness of the deposition layer was determined to be in the region from 2.05 μm to 3.65 μm by FIB-SEM image, which support the ps-LIBS results in the determination of deposition layer thickness. These analyses show that ps-LIBS can be applied to investigate in general wall conditions and plasma-surface interaction processes, thus, fuel retention, material erosion, deposition and components in nuclear fusion devices with high lateral and depth resolution.

Acknowledgements

This work was supported by the National Natural Science Foundation of China (No. 11905049, No. 11875023, No.11904241), Department of Science and Technology of Sichuan Province (No. 2020YJ0181), National MCF Energy R&D Program (No. 2018YFE0303101, 2019YFE03080300), Deutsche Forschungsgemeinschaft (No. 410415657), the Joint Sino-German Research Project (NSFC-DFG) and OPCP-Helmholtz postdoc fellowship. This work has been carried out within the framework of the EUROfusion Consortium and has received funding from the Euratom research and training programme 2014-2018 and 2019-2020 under grant agreement

No 633053. The views and opinions expressed herein do not necessarily reflect those of the European Commission.

ORCID iDs

D. Zhao https://orcid.org/0000-0003-0387-4961
S. Brezinsek https://orcid.org/0000-0002-7213-3326
R. Yi https://orcid.org/0000-0002-4422-5178
J. Oelmann https://orcid.org/0000-0002-0845-4571
L. Cai https://orcid.org/0000-0002-7990-3282
G. Sergienko https://orcid.org/0000-0002-1539-4909
M. Rasinski https://orcid.org/0000-0001-6277-4421
M. Mayer https://orcid.org/0000-0002-5337-6963

References

[1] Klinger T. *et al* 2019 *Nucl. Fusion* **59** 112004
[2] Dhard C. *et al* 2017 *Phys. Scr.* **T170** 014010
[3] Goriaev A. *et al* 2020 *Phys. Scr.* **T171** 014063
[4] Fuchert G. *et al* 2020 *Nucl. Fusion* **60** 036020
[5] Wang E. *et al* 2020 *Phys. Scr.* **T171** 014040
[6] Sereda S. *et al* 2020 *Nucl. Fusion* **60** 086007
[7] Dhard C P. *et al* 2019 *Fusion Eng. Des.* **146** 242
[8] Ruset C. *et al* 2009 *Fusion Eng. Des.* **84** 1662
[9] Mayer M. *et al* 2020 *Phys. Scr.* **T171** 014035
[10] Zhao D. *et al* 2020 *Phys. Scr.* **T171** 014018
[11] Philipps V. *et al* 2013 *Nucl. Fusion* **53** 093002
[12] Semerok A, C Grisolia 2013 *Nucl. Instrum. Methods Phys. Res. Sect. A-Accel. Spectrom. Dect. Assoc. Equip.* **720** 31
[13] Maurya G S. *et al* 2020 *J. Nucl. Mater.* 152417
[14] Li C. *et al* 2019 *Spectroc. Acta Pt. B-Atom. Spectr.* **160** 105689
[15] Yi R. *et al* 2020 *Appl. Surf. Sci.* **532** 147185
[16] Zhao D. *et al* 2018 *Nucl. Instrum. Methods Phys. Res. Sect. B-Beam Interact. Mater. Atoms* **418** 54
[17] Zhao D. *et al* 2020 *Nucl. Fusion* **61** 016025
[18] Xiao Q. *et al* 2015 *J. Nucl. Mater.* **463** 911
[19] Zhao D. *et al* 2018 *Rev. Sci. Instrum.* **89** 073501
[20] Cai L. *et al* 2019 *Rev. Sci. Instrum.* **90** 053503
[21] Almaviva S. *et al* 2020 *Fusion Eng. Des.* **157** 111685
[22] Hubeny M. *et al* 2019 *Nucl. Mater. Energy* **18** 77
[23] Oelmann J. *et al* 2019 *Nucl. Mater. Energy* **18** 153
[24] Grisolia C. *et al* 2007 *J. Nucl. Mater.* **363** 1138
[25] Schweer B. *et al* 2009 *Phys. Scr.* **2009** 014008
[26] Karhunen J. *et al* 2015 *J. Nucl. Mater.* **463** 931
[27] Maurya G S. *et al* 2016 *Spectroc. Acta Pt. B-Atom. Spectr.* **126** 17
[28] Maurya G S. *et al* 2014 *Phys. Scr.* **89** 075601
[29] Paris P. *et al* 2015 *Fusion Eng. Des.* **98** 1349
[30] Almaviva S. *et al* 2016 *Phys. Scr.* **2016** 014043
[31] Sun L. *et al* 2021 *Fusion Eng. Des.* **173** 112811
[32] Zhao D. *et al* 2020 *J. Anal. At. Spectrom.* **35** 2867
[33] Zhao D. *et al* 2020 *Fusion Eng. Des.* **151** 111379
[34] Roldán A M. *et al* 2021 *Fusion Eng. Des.* **172** 112898
[35] Li C. *et al* 2017 *Phys. Scr.* **2017** 014004
[36] Brezinsek S. *et al* 2021 *Nucl. Fusion* **62** 016006
[37] Dhard C. *et al* 2020 *Phys. Scr.* **T171** 014033
[38] Motojima G. *et al* 2020 *Phys. Scr.* **T171** 014054
[39] Brakel R. *et al* 2018 *Proc. 27th IAEA Fusion Energy Conf, India*
[40] Gao Y. *et al* 2019 *Nucl. Fusion* **59** 106015
[41] Gao Y. *et al* 2019 *Nucl. Fusion* **59** 066007
[42] Oelmann J. *et al* 2021 *Nucl. Mater. Energy* **26** 100943